Research Square

Preprints are preliminary reports that have not undergone peer review.
They should not be considered conclusive, used to inform clinical practice,
or referenced by the media as validated information.

Analysis of Mechanical Properties and Instability Influencing Factors of X-shaped Jointed Rock Mass

Shuaitao Wu
Nanyang Institute of Technology
Heng Zhang
hzhangcumt@126.com
Nanyang Institute of Technology
Chenglong Wei
East China University of Technology
Cheng Zhu
China University of Mining and Technology
Xiangqian Chen
Nanyang Institute of Technology
Haolai Xue
Nanyang Institute of Technology
Aobo Li
Nanyang Institute of Technology

Article

Keywords: X-shaped joint, Mechanical properties, Destabilizing factors, Crack propagation patterns

Posted Date: March 30th, 2026

DOI: https://doi.org/10.21203/rs.3.rs-9196589/v1

License: This work is licensed under a Creative Commons Attribution 4.0 International License.
Read Full License

Additional Declarations: No competing interests reported.

Analysis of Mechanical Properties and Instability Influencing Factors of X-shaped Jointed Rock Mass

Shuaitao Wu [1,2], Heng Zhang [1,*], Chenglong Wei [3], Cheng Zhu [4,5], Xiangqian Chen [1], Haolai Xue [1], Aobo Li [1]

[1] *School of Civil Engineering, Nanyang Institute of Technology, Nanyang, Henan 473004, PR China*

[2] *Henan International Joint Laboratory of Dynamics of Impact and Disaster of Engineering Structures, Nanyang Institute of Technology, Nanyang, Henan 473004, PR China*

[3] *College of Civil and Construction Engineering, East China University of Technology, Nanchang, Jiangxi 330013,* PR China

[4] *Huaibei Mining Co., Ltd., Huaibei 235000, PR China*

[5] *School of Mines, China University of Mining and Technology, Xuzhou 221116, PR China;*

The Corresponding author:

Heng Zhang, Email: hzhangcumt@126.com

Abstract: This study delves into the mechanical behavior and fracture propagation mechanism of X-shaped jointed rock masses. It is found that the damage of X-joints leads to stress concentration at the joint tips, which promotes the propagation of fractures along the direction of the maximum principal tensile stress, eventually causing the rock mass to fail along the joint surfaces or at an angle of $\theta_0 = \frac{\pi}{4} + \frac{\varphi_0}{2}$. Under the influence of X-shaped joints, shear fractures in the rock mass increase rapidly in the initial stage of loading and then transform into tensile fractures. These tensile fractures continue to propagate and coalesce into a connected fracture network, significantly weakening the structural integrity and mechanical strength of the rock mass. The uniaxial compressive strength of X-shaped jointed rock masses shows a negative correlation with the length of secondary joints. An increase in the length of secondary joints actually expands the initial damage area in the rock mass and exacerbates the tip stress concentration effect, thereby reducing the overall bearing stiffness and strength of the rock mass. With the increase of the included angle β between primary and secondary joints, the compressive strength exhibits a nearly "M-shaped" variation, reflecting the anisotropic influence of the spatial geometric configuration of joints on rock mass strength. Regarding the included angle α between the primary joints and the loading direction, within the range of $0° \le \alpha \le 15°$, the rock mass strength increases slowly with the increase of α; while within the range of $15^o \le \alpha \le 90^o$, the strength decreases rapidly with the increase of α. The research findings deepen the understanding of the failure mechanism of jointed rock masses and provide a theoretical basis for engineering site selection and disaster reduction decision-making.

Keywords: X-shaped joint; Mechanical properties; Destabilizing factors; Crack propagation patterns

0 Introduction

Owing to the effects of diagenesis and subsequent geological processes, natural rock masses commonly contain various structural planes such as joints and fractures [1,2]. These structural planes intersect to form complex joint networks, leading to the discontinuity, heterogeneity, and anisotropy of engineering rock masses [3]. Joints exhibit diverse morphological characteristics, and their mechanical behaviors and failure features differ significantly. Among various joint types, X-shaped joints represent one of the typical structures in fractured rock masses [4]. The propagation and failure of X-shaped joints are accompanied by a notable crack-tip effect, which exerts a considerable influence on the strength and stability of rock masses [5,6]. Therefore, investigations into the mechanical properties and fracture evolution of X-shaped joints can provide a reliable and effective theoretical foundation for site selection and disaster prevention in engineering projects involving complex jointed rock masses.

In recent years, many scholars have carried out in-depth investigations into the effects of parameters such as joint morphology, joint inclination angle, and joint quantity on the mechanical behavior and fracture evolution of jointed rock masses [7-9]. Akbardoost et al. [10] adopted an incremental approach to predict crack propagation trajectories in rock specimens containing U-shaped, V-shaped end holes, and keyhole-shaped notches. Peng et al. [11] analyzed the displacement field of disc specimens based on fracture mechanics, revealing the influences of joint angle and normal stress on the propagation of wing cracks and secondary coalescence between en-echelon rock joints. Pan et al. [12] discussed the effects of joint inclusions on the dynamic responses of rock-like materials in terms of dynamic strength, energy dissipation, and mesoscopic damage. Liu et al. [13] examined the propagation process of joint fractures varying with inclination angle and uncovered the mesoscopic laws governing crack propagation and failure evolution. Li et al. [14] pointed out that, with an increase in joint inclination angle, the failure mode of rock masses with parallel double joints transitions from tensile and shear failure to conjugate shear failure.

Moreover, researchers have developed sophisticated and advanced numerical methods to simulate the crack propagation mechanisms and failure processes of jointed rock masses [15-17]. Meng and Liu [18] adopted the finite-element-based RFPA software to study complex fracture

mechanics problems in rock masses. Wu et al. [19] and Yu et al. [20] explored the influences of different horizontal distances between holes and fracture centroids on the brittleness of rocks and the mechanical properties of pre-fractured rock materials. Wang et al. [21] examined the effects of rock bridge length on the fatigue strength, volumetric deformation, and fatigue life of rock masses under cyclic uniaxial variable-frequency loading. Dong et al. [22] performed a series of uniaxial compression tests to investigate the influences of sawtooth interface parameters on the fracture behavior of rock-like composite specimens. Wang et al. [23] used PFC3D numerical simulation to study the effects of different fissure intersection angles and fissure lengths on the macroscopic mechanical behavior, crack evolution law, ultimate failure mode, and final crack distribution of pre-flawed rock-like specimens.

In summary, scholars have carried out extensive and in-depth investigations into the failure process of jointed rock masses, and the weakening effect of joints on rock mass strength has been well documented. Existing studies have revealed the significant influences of various joint parameters on the mechanical properties and crack propagation laws of jointed rock masses, greatly advancing the understanding of instability mechanisms in jointed rock mass engineering. However, studies focusing on intersecting X-shaped joints remain relatively limited, especially investigations concerning the effects of key geometric parameters: the length of secondary joints, the angle between primary and secondary joints, and the angle between the loading direction and the primary joint. Therefore, this paper adopts theoretical analysis and UDEC numerical simulations to investigate the mechanical properties and fracture evolution laws of X-shaped jointed rock masses. The research findings contribute to a better understanding of the failure modes and mechanical characteristics of jointed rock masses, and can provide a theoretical reference for engineering site selection and disaster prevention in rock engineering.

1 Mechanical mechanism of failure and instability

1.1 Establishment of mechanical models

To investigate the failure and instability characteristics of X-shaped jointed rock masses, the X-shaped joint structure was decomposed into two individual jointed rock masses based on the single structural plane theory, and these two single-fracture rock masses were adopted as the analytical model, as illustrated in Figure 1. AB and CD represent the primary joint and secondary

joint; σ_1 and σ_3 are the maximum and minimum principal stresses; $\sigma_{\theta 1}$ and $\sigma_{\theta 2}$ represents the normal stress borne by the rock mass structural plane; $\tau_{\theta 1}$ and $\tau_{\theta 2}$ represents the shear stress borne by the rock mass structural plane; θ_1 and θ_2 represents the angle between the joint and the horizontal plane.

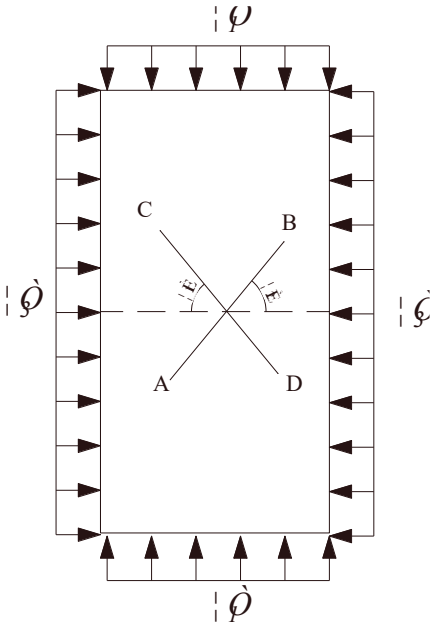


Figure 1 Planar mechanical model of X-shaped jointed rock mass

1.2 Analysis of deformation and instability characteristics

The X-shaped jointed rock mass model is presented in the figure above. Assuming that the biaxial stress satisfies the condition $\sigma_3 = \gamma\sigma_1 = \gamma\sigma$, under the action of far-field stress, the normal stress $\sigma_{\theta 1}$ and tangential stress $\tau_{\theta 1}$ on the jointed surface with an inclination of θ_1 and the normal stress $\sigma_{\theta 2}$ and tangential stress $\tau_{\theta 2}$ on the jointed surface with an inclination of θ_2 are respectively.

$$\begin{cases} \sigma_{\theta 1} = \sigma\left(\cos^2\theta_1 + \gamma\sin^2\theta_1\right) \\ \sigma_{\theta 2} = \sigma\left(\cos^2\theta_2 + \gamma\sin^2\theta_2\right) \\ \tau_{\theta 1} = \sigma\left(1-\gamma\right)\sin\theta_1\cos\theta_1 \\ \tau_{\theta 2} = \sigma\left(1-\gamma\right)\sin\theta_2\cos\theta_2 \end{cases} \tag{1}$$

In the Equation: $\tau_{\theta 1}$ and $\tau_{\theta 2}$ are respectively the shear stresses of the joint plane with an inclination of θ_1 and θ_2, when the interference effect of the intersecting structural plane is not considered; $\sigma_{\theta 1}$ and $\sigma_{\theta 2}$ are the normal stresses at each angle when the mutual interference effect of

the intersecting structural planes is not taken into account.

When the interaction between intersecting structural planes is neglected, the effective shear driving force that induces shear deformation along the structural planes can generally be expressed by the Kalhaway equation [24]:

$$\begin{cases} \tau_{\theta 1}^{e} = \dfrac{K_S \tau_{\theta 1}^{\mathrm{m}} l_{\theta 1}/2a}{\tau_{\theta 1}^{\mathrm{m}} + K_S l_{\theta 1}/2a} \\ \tau_{\theta 2}^{e} = \dfrac{K_S \tau_{\theta 2}^{\mathrm{m}} l_{\theta 2}/2b}{\tau_{\theta 2}^{\mathrm{m}} + K_S l_{\theta 2}/2b} \end{cases} \tag{2}$$

In the Equation: K_S is the initial shear modulus of the structural plane where the jointed rock mass intersects; a and b represent the inclinations and the joint half-lengths respectively; $\tau_{\theta 1}^{e}$ and $\tau_{\theta 2}^{e}$ are the ultimate shear stresses between the intersecting structural planes of the joints with angles of θ_1 and θ_2, respectively; $l_{\theta 1}$ and $l_{\theta 2}$ Shear displacements of the structural planes where the joints intersect at an angle of θ_1 and θ_2, respectively.

When the interaction between the primary and secondary joints is neglected, the horizontal displacements induced by the two joint planes can be derived from Equation (2):

$$\begin{cases} l_{\theta 1}^{-} = \dfrac{2a\tau_{\theta 1}^{e}\tau_{\theta 1}^{m}\cos\theta_1}{K_S\tau_{\theta 1}^{m} - K_S\tau_{\theta 1}^{e}} \\ l_{\theta 2}^{-} = \dfrac{2b\tau_{\theta 2}^{e}\tau_{\theta 2}^{m}\cos\theta_2}{K_S\tau_{\theta 2}^{m} - K_S\tau_{\theta 2}^{e}} \end{cases} \tag{3}$$

Regarding the ultimate shear stresses $\tau_{\theta 1}^{m}$ and $\tau_{\theta 2}^{m}$ of the joint plane in Equation (3), the plane containing the joint consists of both throughgoing and non-throughgoing segments. The shear failure criterion for the joint plane is that the shear stress acting on the plane exceeds the shear strength of the rock mass. The shear strength of the structural plane is derived from the weighted average of the frictional and cohesive strengths of the throughgoing and non-throughgoing segments. According to the Mohr–Coulomb failure criterion, we have:

$$\begin{cases} \tau_{\theta 1}^{m} = \lambda_{\theta 1}\mu_j\sigma_{\theta 1} + \left(1-\lambda_{\theta 1}\right)\mu_r\sigma_{\theta 1} + \left(1-\lambda_{\theta 1}\right)c_r^{i} \\ \tau_{\theta 2}^{m} = \lambda_{\theta 2}\mu_j\sigma_{\theta 2} + \left(1-\lambda_{\theta 2}\right)\mu_r\sigma_{\theta 2} + \left(1-\lambda_{\theta 2}\right)c_r^{i} \end{cases} \tag{4}$$

In the Equation: $\lambda_{\theta 1}$ and $\lambda_{\theta 2}$ are respectively the joint penetration degrees with an

inclination angle of θ_1 and θ_2; μ_j is the friction coefficient of the joint surface; μ_r is the mass friction coefficient of the rock block; c_r^i is the cohesion of the frozen rock mass.

To simplify the analysis, the mutual interference effects are characterized by the inclination angle relationship between the primary and secondary joints. The actual effective sliding driving stress acting on the primary joint surface under the interaction between the primary and secondary joints [26] can be expressed as:

$$\tau_{\theta 1}^{e^*}=\begin{cases}\tau_{\theta 1}^{e}-\tau_{\theta 2}^{e}\dfrac{[\lambda_{\theta 1}\mu_j\sigma_{\theta 1}+(1-\lambda_{\theta 1})(\mu_r\sigma_{\theta 1}+c_r^{'})-\tau_{\theta 1}^{e}][\lambda_{\theta 2}\mu_j\sigma_{\theta 2}+(1-\lambda_{\theta 2})(\mu_r\sigma_{\theta 2}+c_r^{'})]b\cos\theta_2}{[\lambda_{\theta 2}\mu_j\sigma_{\theta 2}+(1-\lambda_{\theta 2})(\mu_r\sigma_{\theta 2}+c_r^{'})-\tau_{\theta 2}^{e}][\lambda_{\theta 1}\mu_j\sigma_{\theta 1}+(1-\lambda_{\theta 1})(\mu_r\sigma_{\theta 1}+c_r^{'})]a\cos\theta_1} & \left(\theta_2<90^\circ\ \eta\theta_2<\theta_1\right)\\ \tau_{\theta 1}^{e}+\tau_{\theta 2}^{e}\dfrac{[\lambda_{\theta 1}\mu_j\sigma_{\theta 1}+(1-\lambda_{\theta 1})(\mu_r\sigma_{\theta 1}+c_r^{'})-\tau_{\theta 1}^{e}][\lambda_{\theta 2}\mu_j\sigma_{\theta 2}+(1-\lambda_{\theta 2})(\mu_r\sigma_{\theta 2}+c_r^{'})]b\cos\theta_2}{[\lambda_{\theta 2}\mu_j\sigma_{\theta 2}+(1-\lambda_{\theta 2})(\mu_r\sigma_{\theta 2}+c_r^{'})-\tau_{\theta 2}^{e}][\lambda_{\theta 1}\mu_j\sigma_{\theta 1}+(1-\lambda_{\theta 1})(\mu_r\sigma_{\theta 1}+c_r^{'})]a\cos\theta_1} & \left(\theta_2<90^\circ\ \eta\theta_2>\theta_1\right)\\ \tau_{\theta 1}^{e}-\tau_{\theta 2}^{e}\dfrac{[\lambda_{\theta 1}\mu_j\sigma_{\theta 1}+(1-\lambda_{\theta 1})(\mu_r\sigma_{\theta 1}+c_r^{'})-\tau_{\theta 1}^{e}][\lambda_{\theta 2}\mu_j\sigma_{\theta 2}+(1-\lambda_{\theta 2})(\mu_r\sigma_{\theta 2}+c_r^{'})]b\sin\theta_2}{[\lambda_{\theta 2}\mu_j\sigma_{\theta 2}+(1-\lambda_{\theta 2})(\mu_r\sigma_{\theta 2}+c_r^{'})-\tau_{\theta 2}^{e}][\lambda_{\theta 1}\mu_j\sigma_{\theta 1}+(1-\lambda_{\theta 1})(\mu_r\sigma_{\theta 1}+c_r^{'})]a\cos\theta_1} & \left(\theta_2>90^\circ\ \eta\theta_2>\theta_1\right)\end{cases} \quad (5)$$

As rock is a brittle material whose tensile strength is much lower than its shear strength, the driving stress within the rock mass causes cracks to propagate along the direction of the maximum circumferential stress at the joint tip. Under this condition, the relationship between the driving stress in the rock mass and the mode-I stress intensity factor at the primary joint tip is given by:

$$K_1^e=\frac{3}{2}\tau_a^{e^*}\sqrt{\pi c}\cos\theta\cos\frac{\theta}{2} \quad (6)$$

θ denotes the crack initiation and propagation angle inclined at a certain angle to the joint. It can be seen from Equation (6) that crack propagation occurs when the mode-I stress intensity factor at the tip of the primary joint exceeds the fracture toughness of the rock [27].

For the instability assessment of X-shaped jointed rock mass failure, the shear strength characteristics of the joints can be quantitatively described by the Coulomb strength criterion as follows:

$$\begin{cases}\tau_{\theta 1}=\sigma_{\theta 1}\tan\phi_{\omega 1}+c_{\omega 1}\\ \tau_{\theta 2}=\sigma_{\theta 2}\tan\phi_{\omega 2}+c_{\omega 2}\end{cases} \quad (7)$$

c_ω represents the cohesive force of the joint, and φ_ω denotes the internal friction angle of the joint. By combining Equations (1) and (7), the relationship among σ, θ, c_ω, and φ_ω can be derived as follows:

$$\sigma - \gamma\sigma \frac{2(c_\omega + \gamma\sigma \tan\varphi_\omega)}{(1-\tan\varphi_\omega \cot\theta)\sin 2\theta} = 0 \tag{8}$$

When the principal stress acting on the fractured rock mass satisfies Equation (8), the stress state on the internal structural plane will reach limit equilibrium. If $\theta = 90°$ or $\theta = \varphi_\omega$ under condition $\sigma_1 - \sigma_3 \to \infty$, this indicates that the specimen will not fail along the structural plane under such a stress state. Differentiating Equation (8) with respect to θ and setting the first derivative to zero, the condition corresponding to the minimum value of σ_1 can be obtained as follows:

$$\tan 2\theta = -\cot\varphi_\omega \to \theta = \frac{\pi}{4} + \frac{\varphi}{2} \tag{9}$$

At this point, the Mohr stress circle is tangent to the strength envelope of the structural plane, as illustrated in Figure 2.

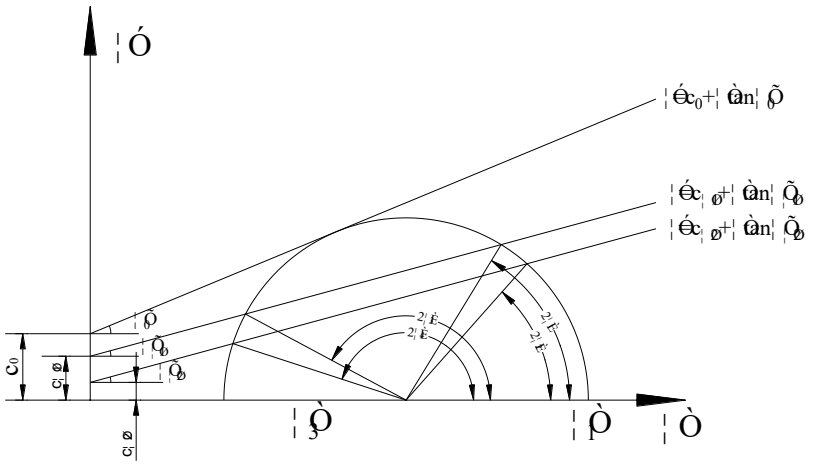


Figure 2 Strength analysis of X-shaped jointed rock mass

As illustrated in Figure 2, lines $\tau = \sigma\tan\varphi_{\omega 1} + c_{\omega 1}$ and $\tau = \sigma\tan\varphi_{\omega 2} + c_{\omega 2}$ represent the strength envelopes of the joint surfaces, and line $\tau = \sigma\tan\varphi_0 + c_0$ denotes the strength envelope of the intact rock. According to the Mohr strength theory, the rock mass fails along the first set of joints when the angle θ between these joints and the horizontal direction satisfies condition $2\theta_1 \le 2\theta \le 2\theta_3$. The rock mass does not fail along the first set of joints when condition $2\theta \ge 2\theta_3$ or $2\theta \le 2\theta_1$ is met. If the angle θ' between the second set of joints

$2\theta_2 \le 2\theta' \le 2\theta_4$ and the horizontal direction satisfies the corresponding criterion at this stage, the rock mass will fail along the second set of joints.

When the stress state points corresponding to both sets of structural planes lie below their respective strength envelopes, i.e., under conditions $2\theta \ge 2\theta_3$ or $2\theta \le 2\theta_1$ and $2\theta' \ge 2\theta_4$ or $2\theta' \le 2\theta_2$, the rock mass does not fail along either set of joints, but instead fractures along the plane oriented at the following angle.

$$\theta_0 = \frac{\pi}{4} + \frac{\varphi_0}{2} \tag{10}$$

2 UDEC numerical model construction

To investigate the mechanical properties of X-shaped jointed rock masses under uniaxial compression, a numerical model of rock masses with pre-existing X-shaped joints was established using the UDEC numerical simulation software. The model was designed with a height of 100 mm and a width of 50 mm. The primary joint has a length of 40 mm, while the secondary joint is 20 mm long. The angle α between the primary and secondary joints, and the angle β between the primary joint and the loading direction, were defined as key variables, with the X-shaped joint positioned at the center of the model, as illustrated in Figure 3.

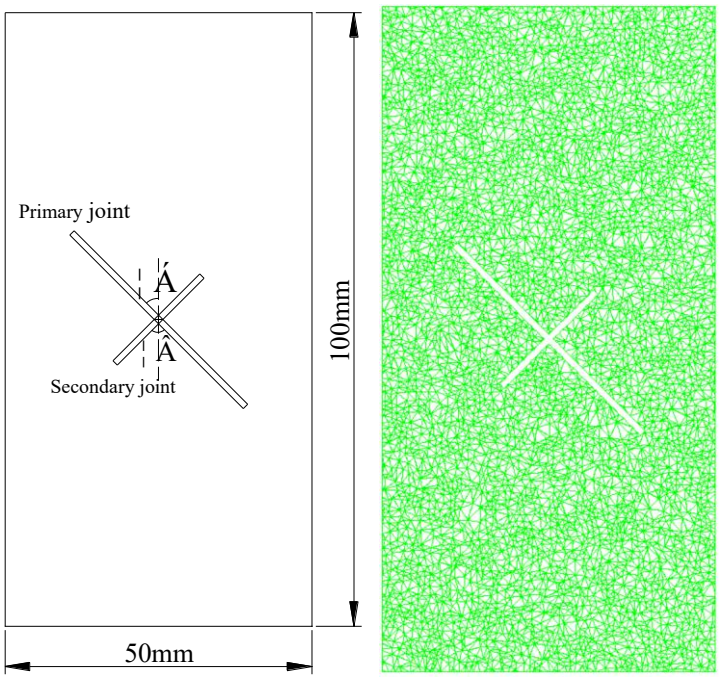


Figure 3 Simulation of X-shaped jointed rock mass

The model was discretized into triangular blocks connected by joint planes. The blocks

adopted a linear elastic constitutive model, with the corresponding parameters presented in Table 1. The joint planes between triangular blocks were modeled using the Mohr-Coulomb constitutive model with residual strength. The top, left, and right boundaries of the model were set as free boundaries, allowing for free lateral and vertical deformation, while the bottom boundary was fixed. The joint parameters are listed in Table 2.

Table 1 Block Parameters

Density /Kg/m^3	Elastic modulus /MPa	Poisonby	Volume modulus /MPa	Shear modulus /MPa
2400	7230	0.28	5477	2824

Table 2 Joint Parameters

Internal friction angle /°	Cohesive force /MPa	Tensile strength /MPa	Normal stiffness /N/M	Expansion angle /°
35	4.5	2.8	4488e9	3

To investigate the influence of secondary joint length on the mechanical properties of X-shaped jointed rock masses, five numerical schemes were designed by systematically varying the length of the secondary joints. Six additional schemes were developed to examine the effect of the angle β between the primary and secondary joints on the rock mass mechanical properties, with this angle adjusted sequentially across the schemes. Seven schemes were further established to explore the impact of the angle α between the primary joint and the loading direction on the mechanical properties of X-shaped jointed rock masses, by changing this angle in a stepwise manner. The specific joint parameters for all schemes are presented in Table 3.

Table 3 Simulation Test Scheme

Model	Primary joint /mm	Secondary joint /mm	β / °	α / °
1	40	20	90	45
2	40	25	90	45
3	40	30	90	45
4	40	35	90	45
5	40	40	90	45
6	40	20	15	45
7	40	20	30	45
8	40	20	45	45
9	40	20	60	45
10	40	20	75	45
11	40	20	90	45

12	40	20	90	0
13	40	20	90	15
14	40	20	90	30
15	40	20	90	45
16	40	20	90	60
17	40	20	90	75
18	40	20	90	90

The top, left, and right boundaries of the model are set as free boundary conditions, allowing the specimen to deform freely in the transverse and vertical directions. The bottom is constrained by fixed boundary conditions to restrict its displacement. The loading test in this study adopts a displacement-controlled strategy, with a constant loading rate of 0.05 mm/s. To capture the mechanical response of the model, the "HISTORY" module was employed to record real-time changes in vertical stress and strain, and the software's visualization function was used to dynamically observe the initiation and propagation of fissures. Meanwhile, the "CONFIG" module was utilized to quantitatively detect the accumulation and dissipation of energy within the model.

3 Analysis of failure characteristics

3.1 Stress-strain characteristics

The mechanical response of X-shaped jointed rock masses under uniaxial compression exhibits significant nonlinear characteristics. Its stress-strain behavior is tightly coupled with the crack evolution process, which together reveal the intrinsic mechanism of rock masses from microscopic damage accumulation to macroscopic instability and failure. The stress-strain and crack evolution curve during loading are plotted, as shown in Figure 4.

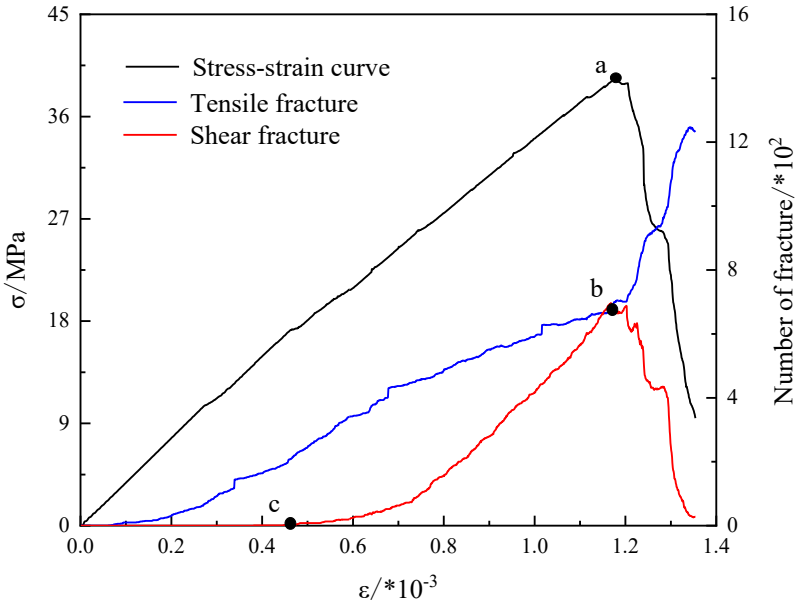


Figure 4 Stress-strain and crack evolution curve

The stress-strain behavior and crack evolution of X-shaped rock masses can be divided into three distinct stages:

(1) Stage A (Elastic Compaction Stage)

During this stage, the stress-strain curve exhibits a linear growth characteristic, and the volumes of tensile cracks and shear cracks remain almost zero. This phenomenon indicates that during the initial loading process, external energy is mainly used to overcome the closure resistance of the original microcracks inside the rock mass. The rock mass skeleton undergoes elastic compressive deformation without generating new damage. The rock mass shows obvious elastic energy storage characteristics, and the accumulated elastic energy provides the driving force for the initiation and propagation of subsequent cracks. Point c marks the critical strain for the initiation of shear cracks, signifying the transition of the rock mass from the elastic stage to the damage stage.

(2) Stage B (Fracture Propagation Stage)

As loading continues, stress and strain rise steadily until reaching the peak point a, at which point the internal damage of the rock mass begins to accumulate at an accelerated pace. Meanwhile, the volume of tensile cracks increases slowly until point b and then grows rapidly; shear cracks initiate at point c and propagate at an increasing rate. From the perspective of damage mechanics, the evolution of cracks dominates the mechanical behavior of the rock mass in this stage: shear cracks initiate first, followed by tensile cracks, leading to the gradual accumulation of internal damage. Point b is the turning point for the rapid propagation of tensile cracks, marking the start of the internal damage spreading from local areas to the entire rock mass. Point a represents the ultimate bearing capacity of the rock mass, at which point an internal crack network has initially formed and the structural integrity of the rock mass is severely compromised. The energy evolution characteristics of this stage indicate that the externally input energy gradually shifts from being stored as elastic strain energy to being consumed as surface energy required for crack propagation, resulting in a gradual decrease in the stability of the rock mass.

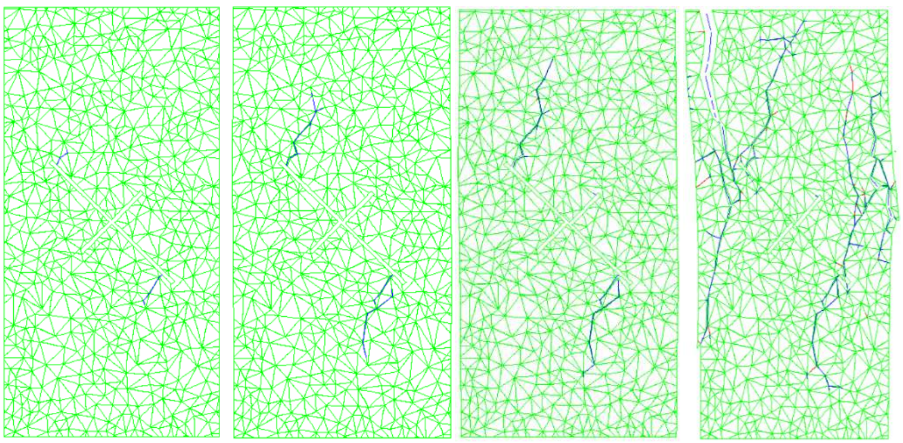
(3) Stage C (Failure Stage)

The stress drops sharply from the peak point a, with the volume of tensile cracks increasing drastically, while the volume of shear cracks rises first and then decreases. This stage corresponds to the formation of a macroscopic failure surface, meaning that cracks connect with each other to form

a through-going fracture surface, after which the rock mass loses its bearing capacity. In the residual stage, the total crack volume tends to stabilize. From the perspective of energy dissipation, a large amount of elastic energy accumulated inside the rock mass is released instantaneously in this stage, converting into kinetic energy and frictional heat, leading to a rapid stress drop. The dominant role of tensile cracks indicates that the final failure of X-shaped jointed rock masses is controlled by the tensile failure mechanism. This tensile failure mode is often accompanied by more intense energy release and more sudden failure characteristics, posing a serious threat to engineering stability.

3.2 Characteristics of fracture evolution

Figure 5 illustrates the dynamic evolution process of crack initiation and propagation during the failure of X-shaped jointed rock masses, intuitively revealing the physical mechanism from microscopic damage accumulation to macroscopic fracture formation. In the initial loading stage, a small number of tensile cracks first appear and then gradually extend, with their distribution range and quantity continuously increasing. This stage corresponds to the tensile crack curve from the start of loading to point b in Figure 4. From the perspective of meso-damage mechanics, since the tensile strength of rock-like materials is much lower than their shear strength, the stress concentration effect at the tips of X-joints first induces tensile failure along the direction of the maximum principal stress. The initiation of these tensile cracks marks the formation of initial internal damage in the rock mass.



(a) cyc40000 (b) cyc80000 (c) cyc120000 (d) cyc160000

Figure 5 Fracture initiation and propagation evolution process (Note: red fractures represent shear fractures, blue fractures represent tensile fractures)

After a period of loading, shear cracks begin to appear and undergo a brief increase in quantity, which is consistent with the shear crack curve from point c to point b in Figure 4. The emergence of

shear cracks indicates a qualitative change in the internal stress state of the rock mass, where stress is transferred and redistributed between joint surfaces through shear slip. However, the growth of shear cracks is temporary. Subsequently, shear cracks transform into tensile cracks, eventually forming a complex tensile crack network, which aligns with the crack count curve from point b to the end of loading in Figure 4.

This crack evolution law profoundly reflects the damage and failure mechanism of X-shaped jointed rock masses: shear cracks develop briefly in the initial stage and quickly transform into tensile cracks, indicating that the internal stress field of the rock mass continuously adjusts and tends toward a tensile failure mode. Overall, tensile cracks continue to develop and dominate the entire evolution process, while shear cracks undergo a brief period of rapid growth before transforming into tensile cracks. The continuous propagation and interconnection of tensile cracks greatly weaken the integrity and structural strength of the rock mass, which is the key factor leading to the final macroscopic instability of the rock mass. Therefore, engineering monitoring should focus on the initiation and propagation characteristics of tensile cracks to effectively evaluate and prevent engineering disasters.

3.3 Energy accumulation and dissipation characteristics

The energy evolution characteristics of rock masses during loading are key indicators for revealing their damage accumulation and instability failure mechanisms. Figure 6 illustrates the energy accumulation and dissipation process of X-shaped jointed rock masses during loading. Throughout the loading process, the externally input energy follows two transformation paths: first, part of the energy is absorbed by the rock mass and converted into compressive strain energy stored internally; second, the remaining energy is dissipated and released in the form of friction work and kinetic energy.

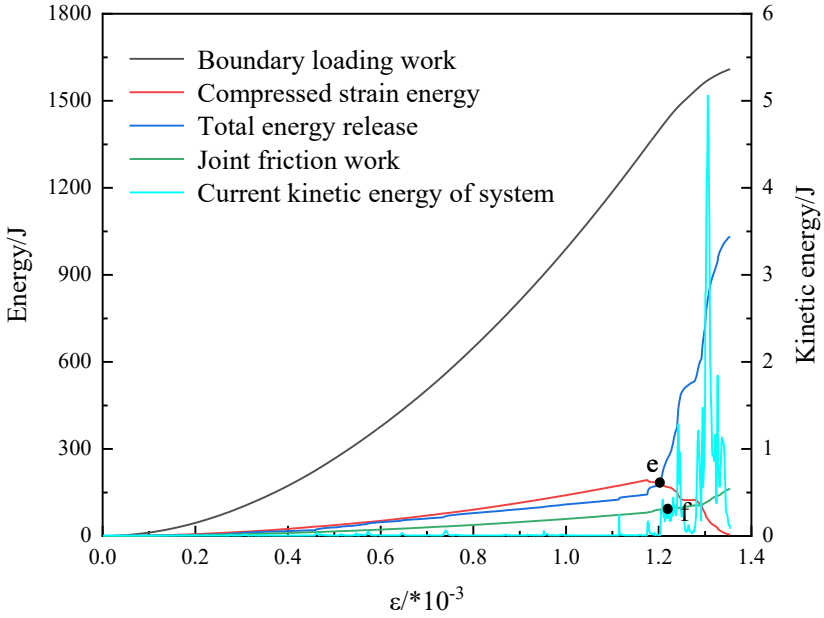


Figure 6 Energy accumulation and dissipation process

From the perspective of energy conversion, the boundary loading work of X-shaped jointed rock masses shows a continuous upward trend throughout the loading process, with its growth rate gradually changing from rapid to stable, reflecting the dynamic process of continuous external energy input. Before point e, the internal compressive strain energy accumulates slowly in the initial stage and then the accumulation rate further decreases. This indicates that in the elastic stage, the input energy is mainly converted into releasable elastic strain energy stored inside the rock mass. From point e to point f, energy release, friction work, and kinetic energy release first show a slow upward trend and then increase sharply. This phenomenon profoundly reveals the energy evolution mechanism before rock mass instability: when the rock mass stress approaches the peak value, internal cracks develop rapidly, the accumulation of stored compressive strain energy slows down, while the energy release rate of friction work driving crack propagation and kinetic energy converted into system energy increases significantly. The abrupt change in this energy distribution mechanism means that the internal damage of the rock mass has reached a critical state, the conversion process from elastic stored energy to dissipated energy intensifies, and eventually leads to the loss of the macroscopic bearing capacity of the rock mass.

4 The influence of joint parameters on the mechanical properties

4.1 Influence of secondary joint length

An increase in secondary joint length has a significant weakening effect on the mechanical

properties of X-shaped jointed rock masses. Figure 7 illustrates the peak strength corresponding to different secondary joint lengths. As the secondary joint length increases, the peak strength shows a downward trend, indicating that the uniaxial compressive strength of X-shaped jointed rock masses gradually decreases with an increase in secondary joint length.

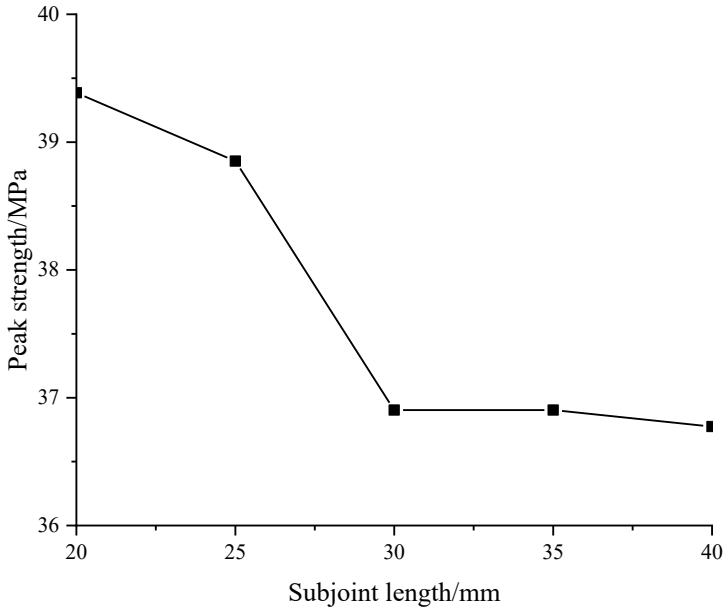


Figure 7 Peak strength corresponding to different secondary joint length

An increase in secondary joint length essentially expands the initial damage zone within the rock mass. As a pre-existing defect inside the rock mass, an increase in the size of secondary joints directly elevates the degree of internal damage, thereby exacerbating the stress concentration effect at the joint tips. This stress concentration is particularly pronounced in the early stage of loading. As the secondary joint length increases from 20 mm to 40 mm, cracks initiate in the rock mass at a lower stress level, leading to a rapid decline in peak strength. When the secondary joint length falls within 20-30 mm, the peak strength drops sharply from approximately 39.4 MPa to 36.9 MPa. This indicates that within this interval, the peak strength is extremely sensitive to changes in secondary joint length, and an increase in secondary joint length results in a significant reduction in peak strength.

Figure 8 presents the stress-strain curves corresponding to different secondary joint lengths. At small strains, the curves are approximately linear, indicating that in the elastic stage, the stress-strain relationship of rock masses with different secondary joint lengths follows Hooke's law.

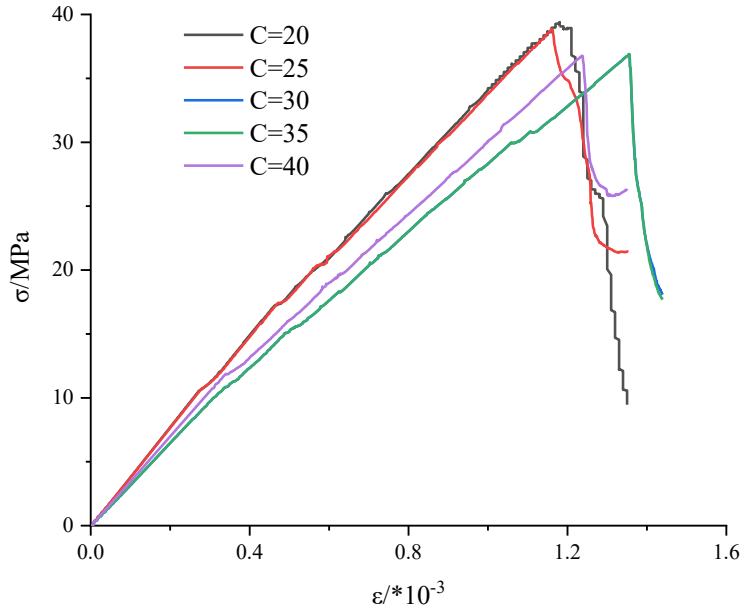


Figure 8 Stress-strain curves corresponding to different secondary joint length

The slope of the curve increases as the secondary joint length decreases, indicating that the elastic modulus of X-shaped jointed rock masses is negatively correlated with the secondary joint length. Shorter secondary joints endow the rock mass with stronger resistance to elastic deformation, whereas an increase in secondary joint length leads to a significant reduction in the rock mass's deformation resistance. From the perspective of energy evolution, an increase in secondary joint length reduces the compressive strain energy accumulated in the rock mass during the elastic stage, while the proportion of dissipated energy used to drive crack propagation and frictional sliding increases relatively. This shift in energy allocation directly results in a decrease in the overall bearing stiffness and strength of the rock mass. As strain increases, the curves enter the plastic phase. The curve with the shortest secondary joint length reaches the highest peak strength. As the secondary joint length increases from 20 mm to 40 mm, the peak strength gradually decreases, which is consistent with the previously observed trend of peak strength varying with secondary joint length.

Furthermore, the secondary joint length also profoundly affects the energy release characteristics and failure modes of the rock mass. Figure 9 presents the total energy release curves corresponding to different secondary joint lengths.

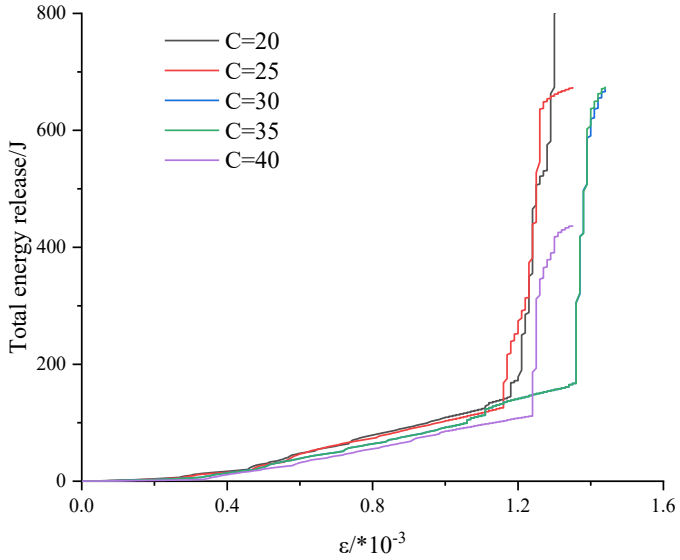


Figure 9 Total energy release corresponding to different secondary joint length

For each curve, the total energy release remains low and grows slowly at small strains. Once the strain exceeds a certain threshold, the curve rises sharply, and the rock mass undergoes rapid destruction with a large amount of energy released. Rock masses with shorter secondary joint lengths ($C = 20$) exhibit sudden and intense energy release processes: the initial growth is extremely slow, followed by a sharp rise, and the stress drops rapidly during failure, showing obvious brittle characteristics. In contrast, as the secondary joint length increases ($C = 40$), the energy release process becomes relatively slow and delayed: the initial increase is the slowest, the sharp rise phase occurs the latest, the final release value is low, and the overall energy release process is the slowest.

4.2 The angle between the primary and secondary joints

Variations in the included angle between primary and secondary joints profoundly influence the mechanical response and energy evolution characteristics of X-shaped jointed rock masses. Figure 10 presents the peak strength corresponding to different included angles between primary and secondary joints. The curve roughly follows an M-shaped distribution: as the included angle changes, the peak strength first decreases, then increases, and finally decreases again.

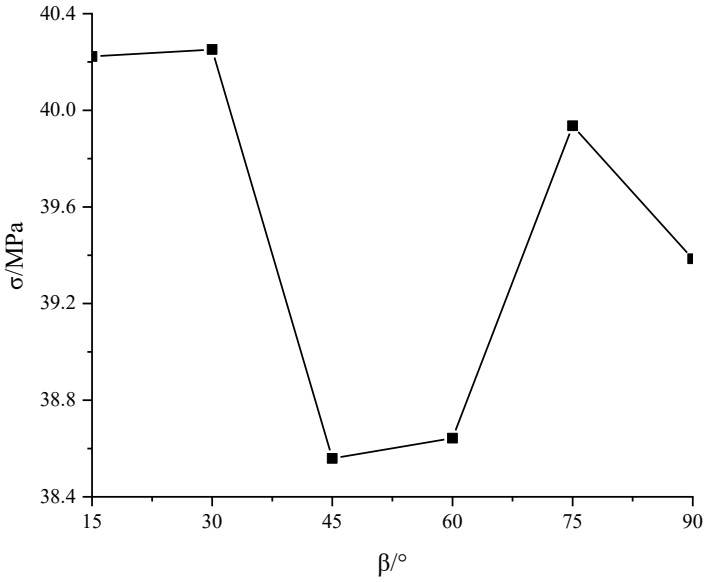


Figure 10 Peak strength corresponding to different β values

This complex non-monotonic variation reveals the anisotropic influence mechanism of joint spatial geometric configuration on rock mass strength. From the perspective of meso-scale damage evolution mechanism, when Parameter β falls within range $15^{o} \le \beta \le 30^{o}$, the peak strength remains basically stable and at a relatively high level. This indicates that the spatial combination of primary and secondary joints within this angular range has a weak weakening effect on rock mass strength, possibly because the primary and secondary joints do not form a continuous shear slip path under this configuration, which limits the expansion of the damage zone. However, when Parameter β enters range $30^{o} \le \beta \le 45^{o}$, the peak strength drops sharply. Combined with the analysis of crack propagation laws, this angular configuration is more conducive to the penetration of cracks between the tips of primary and secondary joints, making shear zones easier to form, thereby significantly reducing the macroscopic strength of the rock mass. When Parameter β reaches range $30^{o} \le \beta \le 75^{o}$, with the continuous increase of the included angle between primary and secondary joints, the peak strength of the rock mass begins to gradually recover and rise, indicating that the shear slip trend of the joint surface weakens under the large-angle configuration, and the bearing capacity of the rock mass is partially restored. When Parameter β reaches value $75^{o} \le \beta \le 90^{o}$, the peak strength decreases again, which reflects another failure mode of the rock mass integrity caused by the nearly orthogonal joint

configuration.

Figure 11 presents the stress-strain curves corresponding to different primary and secondary joint angles.

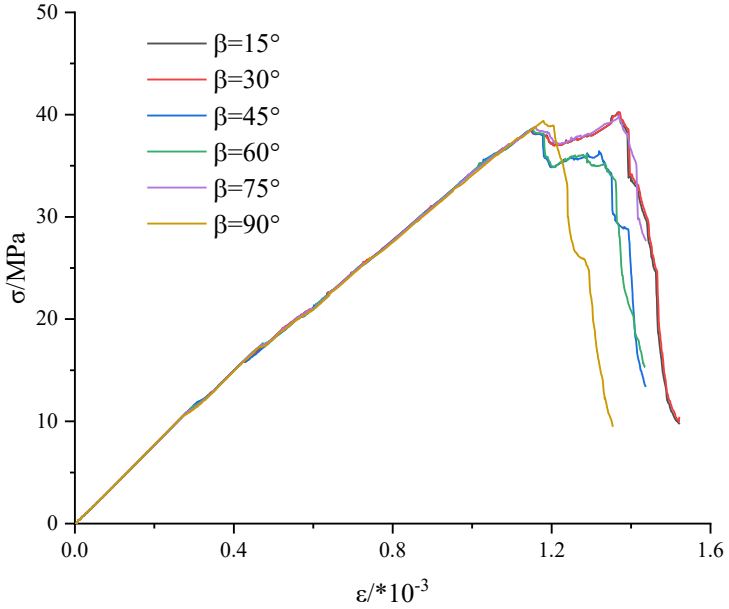


Figure 11 Stress-strain curves corresponding to different β values

At the small strain stage, the slopes of the curves with different values of β are relatively low, indicating that the included angle between primary and secondary joints has little effect on the elastic modulus of the rock mass in the elastic stage, and their ability to resist elastic deformation is roughly similar. As strain increases, the curves enter the plastic stage, and the mechanical responses under different angles show significant differences. When $\beta = 15°$ and $\beta = 30°$, the peak strength is relatively high and the strain at failure is small; when $\beta = 45°$, the peak strength is the lowest, and the specimen enters an obvious plastic deformation stage the earliest. When $\beta = 60°$, $\beta = 75°$, and $\beta = 90°$, the peak strength increases sequentially, accompanied by a gradual increase in the corresponding peak strain. This variation indicates that the included angle between primary and secondary joints not only changes the peak strength of the rock mass but also alters its ductile characteristics.

Furthermore, the included angle between primary and secondary joints exerts a significant control on the energy release characteristics of the rock mass. Figure 12 presents the energy release curves corresponding to different angles between primary and secondary joints.

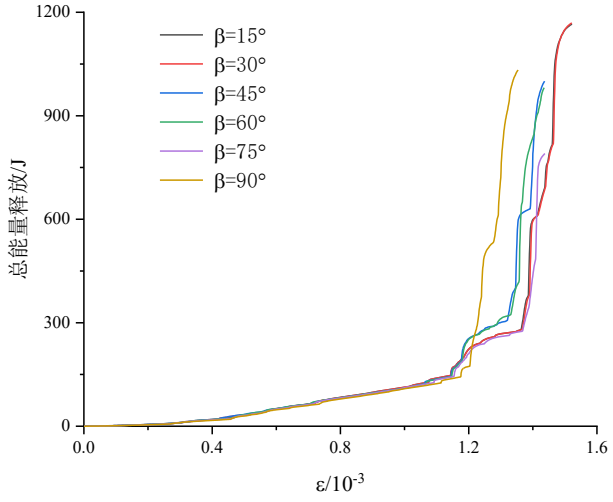


Figure 12 Total energy release corresponding to different β values

When β = 15°, the energy release is slow in the initial stage and then increases sharply with a large slope, indicating that the failure process is rapid and intense, showing strong brittle failure characteristics. When β = 45°, the curve remains stable in the early stage, and the later sharp increase phase occurs relatively late with a smaller slope, corresponding to a relatively slow energy release process. This indicates that the rock mass has a strong energy dissipation capacity under this angular configuration, and the failure process is more ductile. When β = 90°, the energy release starts slowly and then shows a significant sharp increase, with an obvious prominent phase during the failure process. These energy evolution characteristics indicate that changes in the included angle between primary and secondary joints directly affect the failure mode and dynamic response of the rock mass by altering the crack propagation path and energy dissipation mechanism.

4.3 The angle between the primary joint and the loading direction

Variations in the included angle between the primary joint and the loading direction significantly alter the stress transfer paths and crack propagation modes of X-shaped jointed rock masses, leading to strong anisotropy in their mechanical properties.

Figure 13 presents the peak strength corresponding to different values of α. The compressive strength of X-shaped jointed rock masses is significantly correlated with the included angle between the primary joint and the loading direction. As the angle increases to

$0^{o} \le \alpha \le 15^{o}$, the peak strength rises from approximately 50 MPa to nearly 60 MPa. This indicates that within this angular range, the orientation of the primary joint surface facilitates the uniform distribution of internal stress in the rock mass, delaying the stress concentration effect at crack tips and thus causing the peak strength to increase significantly with the rise of α.

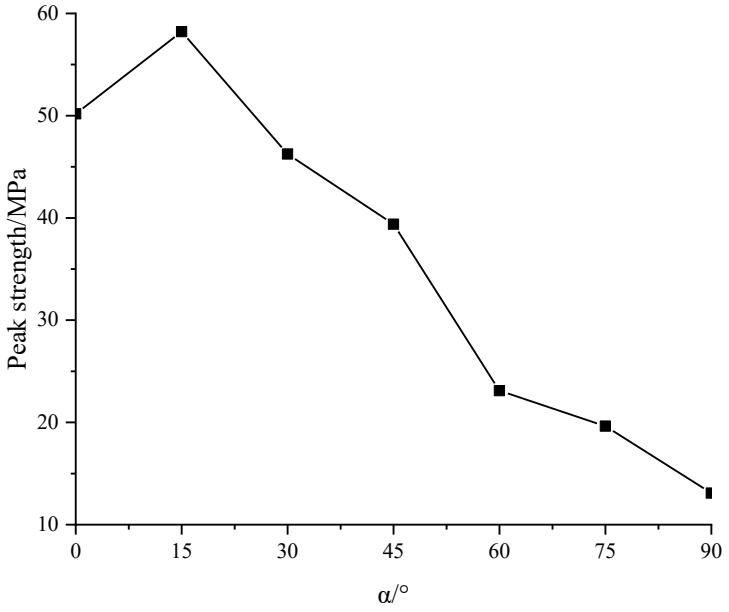


Figure 13 Peak strength corresponding to different α values

Beyond this point, as the angle increases to $15^{o} \le \alpha \le 90^{o}$, the peak strength begins to decrease continuously from about 60 MPa, dropping to approximately 13 MPa at 90°. This sharp attenuation reflects that when the loading direction tends to be perpendicular to the primary joint surface, shear slip along the joint surface becomes the dominant failure mechanism, which greatly weakens the bearing capacity of the rock mass. Therefore, when the angle exceeds 15°, further increases in the included angle between the primary joint and the loading direction result in a continuous and significant decrease in the peak strength of the rock mass, accompanied by a weakening of its ability to resist external loads.

Figure 14 shows the stress-strain curves corresponding to different angles between the main joints and the loading direction.

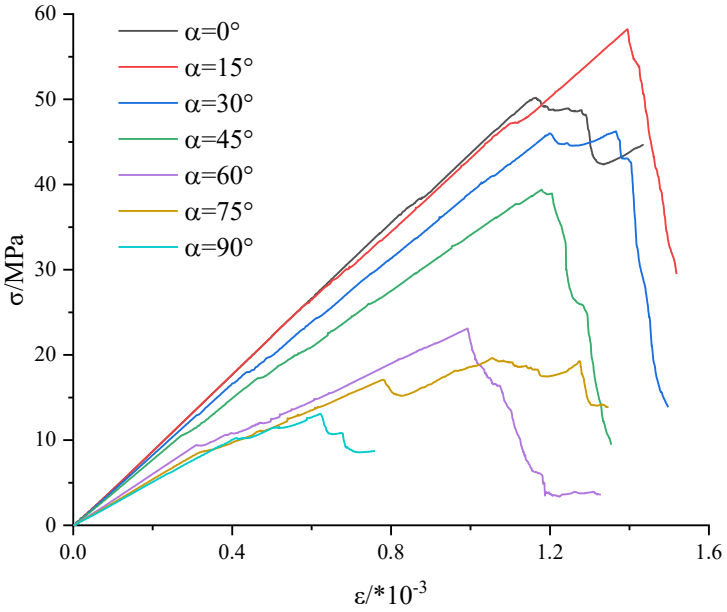


Figure 14 Stress-strain curves corresponding to different α values

In the small strain stage, the slopes of curves $\alpha = 0°$, $\alpha = 15°$ and $\alpha = 30°$ are relatively large, indicating that the rock mass exhibits high elastic modulus and strong resistance to elastic deformation at these angles. In contrast, the slopes of curves $\alpha = 60°$, $\alpha = 75°$ and $\alpha = 90°$ are relatively small, corresponding to weak resistance to elastic deformation. This difference stems from the different constraint effects of joint surfaces on compressive deformation under various angles: at small angles, the rock mass mainly undergoes closure and sliding along the joint surfaces, resulting in high stiffness; at large angles, the joint surfaces tend to open, leading to a decrease in overall stiffness. As strain gradually increases, the curves deviate from the linear elastic stage and enter the plastic deformation stage. The curve reaches its peak point at $\alpha = 15°$, corresponding to the highest peak strength. Within range $15^{o} \le \alpha \le 90^{o}$, the peak strength decreases sequentially, while the corresponding peak strain increases gradually. This phenomenon indicates that as angle α increases, the rock mass gradually transitions from brittle failure to ductile failure. After reaching the peak strength, the stress of each curve drops rapidly. Curves with smaller α values show a steeper decline, indicating that the rock mass failure is more sudden and the stress drops faster. In contrast, curves with larger α values decline more gently, implying a relatively slow and progressive failure process.

Figure 15 illustrates the energy release curves corresponding to different angles between the primary joints and the loading direction.

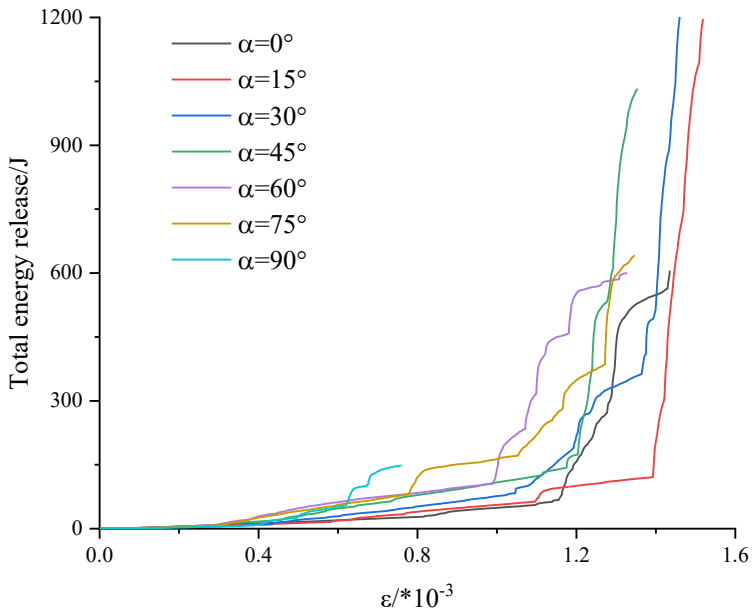


Figure 15 Total energy release corresponding to different α values

At $\alpha = 0°$, the energy release is initially slow, with a moderate upward slope in the later stage, and the evolution process is stable. At $\alpha = 15°$, the early energy release is slow, followed by a steep upward slope in the later stage, and the total energy release is less than that at $\alpha = 30°$. Notably, at $\alpha = 30°$, the curve shows slow initial energy release and a steep upward slope in the later stage, corresponding to the strongest energy release. This indicates that at this angle, the rock mass releases a large amount of elastic energy at the moment of failure, corresponding to the most intense failure behavior. At $\alpha = 45°$, the curve remains stable in the early stage, with the upward slope appearing late and relatively gentle, representing relatively slow energy release. At $\alpha = 90°$, the energy release is initially slow, with an early sharp rise stage but a gentle slope, and the overall energy release level is low. These energy evolution characteristics indicate that as the angle between the main joint and the loading direction increases, the energy release mechanism of the rock mass changes from instantaneous elastic energy release to gradual friction dissipation, and the failure mode gradually transitions from brittle tensile failure to ductile shear slip.

5 Conclusions

(1) Rock is a typical brittle material whose tensile strength is considerably lower than its shear strength. Driving stress induces stress concentration at the joint tips, and cracks propagate along the direction of the maximum circumferential stress. The failure mode of X-shaped joints is affected by the angle between the joint and the horizontal plane, which can be classified into failure propagating

from the joint tips and failure occurring along angle $\theta_0 = \frac{\pi}{4} + \frac{\varphi_0}{2}$.

(2) Under the influence of X-shaped joints, shear fractures in the rock mass increase rapidly at the initial loading stage and then transform into tensile fractures. At the tips of the primary joints, stress concentration first induces the initiation of vertical cracks, which propagate toward the upper and lower surfaces of the specimen. Following the peak stress, the tensile fractures continue to propagate and coalesce into a network of through-going fractures, leading to a substantial degradation in the integrity and strength of the rock mass.

(3) The strength of X-shaped jointed rock mass is negatively correlated with the length of secondary joints; that is, the longer the secondary joints, the lower the strength of the jointed rock mass. With an increase in the angle β between the primary and secondary joints, the strength of the jointed rock mass exhibits an approximately "M-shaped" distribution. For the angle α between the primary joint and the loading direction, within range $0° \le \alpha \le 15°$, the strength of the jointed rock mass increases slowly with the rise of α, whereas beyond angle $15^o \le \alpha \le 90^o$, the strength decreases rapidly as α increases. Therefore, particular attention should be paid to the positional relationship between the engineering structure and the X-shaped jointed rock mass in project site selection and layout.

Data availability

The datasets used and/or analysed during the current study available from the corresponding author on reasonable request.

Conflicts of Interest

The authors declare that they have no known competing financial interests or personal relationships that could have appeared to influence the work reported in this paper.

Research funding

We gratefully wish to acknowledge Sponsored by the National Natural Science Foundation of China (52504133, 52404151) and Natural Science Foundation of Henan (252300423439) and Key Scientific Research Projects for Higher Education of Henan Province (25A130007,26A440011) and Research Project on Science and Technology of Nanyang City (24KJGG018, 24JCQY038, 25JCQY002).

References

[1] Xu H, Zhang Z, Yan J, et al. Study on mechanical properties and failure mechanism of hard rock with stiff discontinuities based on 3D printing. Engineering Failure Analysis, 2024, 161: 108225.

[2] Huang J, Ying YH, Jia CJ et al. Analysis of mechanical properties and failure modes of rock masses with different joint densities via 3D printing. Journal of Hunan University (Natural Sciences) 1-11 [2026-01-08]. https://link.cnki.net/urlid/43.1061.n.20251217.1535.002.

[3] Rong G, Tan J, Zhan H, et al. Quantitative evaluation of fracture geometry influence on nonlinear flow in a single rock fracture. Journal of Hydrology, 2020, 589(1-2): 125162.

[4] Deng ZD, Deng TF, Cao MS, et al. Equivalent elastic model and deformation characteristics of X-Type cross-Jointed rock mass. International Journal of Geomechanics, 2022, 22(7): 04022100.

[5] Hu XM, Liu SY, Liu H, et al. Analysis of Interference Effects and Calculation Model for Crack Initiation Strength in X-Type Jointed Rock Mass After Freeze-Thaw Cycles. Geofluids, 2024, 1: 5177240

[6] Dong ZH, Wang PT, Li P, et al. Dynamic Crack Initiation in Holed and Jointed Rock Masses: A Maximum Energy Release Rate Criterion and Parametric Influences. Rock Mechanics Bulletin. 2025. DOI: 10.1016 / j.r ockmb. 2025.100261.

[7] Kim HE, Kim MS, Yoo, WK, et al. Experimental Investigation on the Effects of Cutting Direction and Joint Spacing on the Cuttability Behaviour of a Conical Pick in Jointed Rock Mass. Applied Sciences-Basel, 2025, 15(8): 4347.

[8] Wang W, Shen WF, Cao YJ, et al. Uniaxial Compression Behavior and Energy Evolution of Joint Rock Repaired and Reinforced with Biocementation Method. Rock Mechanics and Rock Engineering, 2025, 58(3):3371-3390.

[9] Agosti A, Cylwik SD, Utili S. Optimal mine pitwall profiles in jointed anisotropic rock masses. International Journal of Mining Reclamation and Environment, 2025, 39(3): 210-234.

[10] Akbardoost J, Torabi A R, Amani H. Predicting the fracture trajectory in U, VO, and key-hole notched specimens using an incremental approach. Engineering Fracture Mechanics, 2018, 200: 189-207.

[11] Peng J, Wang ZX, Wang, LF, et al. Influence of Inclination of En-Echelon Joints on Shearing Behavior of Crystalline Rock. International Journal for Numerical and Analytical Methods in

Geomechanics, 2025, 49(14): 3232-3250.

[12] Pan B, Wang XG, Xu ZY, et al. Experimental and numerical study of fracture behavior of rock like material specimens with single pre-set joint under dynamic loading. Materials, 2021,14 (10): 2690 2690.

[13] Liu L, Li H, Li X et al. Underlying mechanisms of crack initiation for granitic rocks containing a single pre-existing flaw: insights from digital image correlation (DIC) analysis. Rock Mechanics and Rock Engineering, 2020, 54(2): 857-873.

[14] Li H, Yang SQ, Yang Z, et al. Experimental and numerical study on the mechanical behaviors and crack propagation of sandstone containing two parallel fissures. Theoretical and Applied Fracture Mechanics, 2023, 126: 103965.

[15] Erarslan N. Microstructural investigation of subcritical crack propagation and Fracture Process Zone (FPZ) by the reduction of rock fracture toughness under cyclic loading. Engineering Geology, 2016, 208: 181-190.

[16] Wang X, Jiang Y, Li B. Experimental and numerical study on crack propagation and deformation around underground opening in jointed rock masses. Geosciences Journal, 2017, 21(2): 291-304.

[17] Zeng W, Yang SQ, Tian WL. Experimental and numerical investigation of brittle sandstone specimens containing different shapes of holes under uniaxial compression. Engineering Fracture Mechanics, 2018, 200: 430-450.

[18] Meng X, Liu W. Study on Failure Process and Permeation Evolution of Single-Cracked Rock[J]. Advances in Materials Science and Engineering, 2018, 2018(1): 7915652.

[19] Wu T, Gao Y, Zhou Y, et al. Experimental and numerical study on the interaction between holes and fissures in rock-like materials under uniaxial compression. Theoretical and Applied Fracture Mechanics, 2020, 106: 102488.

[20] Yu J, Yao Y, Wang K, et al. Experimental investigation of effects of multi-fissures on brittleness of ordinary Portland cement concrete and rubberized concrete. Engineering Fracture Mechanics, 2024, 306: 110254.

[21] Wang Y, Yang H N, Han J Q, et al. Effect of rock bridge length on fracture and damage modelling in granite containing hole and fissures under cyclic uniaxial increasing-amplitude decreasing-frequency (CUIADF) loads. International Journal of Fatigue, 2022, 158: 106741.

[22] *Dong T, Cao P, Wang F, et al. Strain field evolution and crack coalescence mechanism of composite strength rock-like specimens with sawtooth interface. Theoretical and Applied Fracture Mechanics, 2023, 126: 103947.*

[23] *Wang H, Gao Y, Zhou Y. Experimental and numerical studies of brittle rock-like specimens with unfilled cross fissures under uniaxial compression. Theoretical and Applied Fracture Mechanics, 2022, 117: 103167.*

[24] *Shen QQ, Xiang LL, You CH, et al. Fracture mechanism of red sandstone with cross-crack: based on the new cross-crack propagation criterion and DIC technique. Rock Mechanics and Rock Engineering, 2026, 59: 2211-2227.*

[25] *Liu SY. Experimental investigation on mechanical properties and fracture damage modeling of frozen X-shaped jointed rock masses. Jiangxi University of Science and Technology, 2025.*

[26] *Lee S, Ravichandran G. Crack initiation in brittle solids under multiaxial compression. Engineering Fracture Mechanics, 2003, 70 (13): 1645-1658.*

[27] *Zhou QJ, Fu YH, Wang GS, et al. Experimental study on mechanical properties and failure mechanism of symmetrical X - type fractured rock mass. Nonferrous Metals Engineering, 2023, 13: 110-119.*